Available online at www.sciencedirect.com
ScienceDirect
Trans. Nonferrous Met. Soc. China 35(2025) 4230−4241
Transactions of Nonferrous Metals Society of China
www.tnmsc.cn

Effects of zirconia coating on improvement of sodium-ion migration in $NaNi_{1/3}Fe_{1/3}Mn_{1/3}O_2$ cathodes for sodium-ion batteries

Wei-jia TANG[1,2,3], Yun-jiao LI[1,2,3], Yu-ming LIU[1,2,3], Chang-long LEI[1,2,3], Shi-jie JIANG[1,2,3], Zhen-jiang HE[1,2,3]

1. School of Metallurgy and Environment, Central South University, Changsha 410083, China;
2. Advanced Battery Materials Engineering Research Center of the Ministry of Education, Central South University, Changsha 410083, China;
3. National Engineering Research Center of Low-carbon Nonferrous Metallurgy, Central South University, Changsha 410083, China

Received 18 March 2024; accepted 15 November 2024

Abstract: To investigate the mechanism by which ZrO_2 modification affects the electrochemical performance of the $NaNi_{1/3}Fe_{1/3}Mn_{1/3}O_2$ (NFM) cathode material for sodium-ion batteries, ZrO_2-coated NFM (ZrO_2@NFM) was prepared via high-temperature calcination. XRD refinement results revealed that ZrO_2 modification increased the Na-layer spacing in the NFM material. XPS analysis results demonstrated that ZrO_2 modification adjusted the Mn^{3+}/Mn^{4+} ratio in NFM by reducing the Mn^{3+} content. Electrochemical test results revealed that, compared to NFM, ZrO_2@NFM exhibited superior rate capability and cycling stability. It also exhibited significantly enhanced Na^+ diffusion coefficients and reduced interfacial charge transfer resistance. The ZrO_2 coating increased Na-layer spacing, reduced electrochemical polarization, and inhibited side reactions. In summary, the synergistic effect of component regulation and surface engineering through ZrO_2 coating improved Na^+ diffusion kinetics and enhanced cycling stability.
Key words: sodium-ion battery; ZrO_2 coating; layered oxide cathodes; diffusion coefficient; electrochemical performance

1 Introduction

Sodium-ion battery (SIB) technology offers an efficient, economical, and sustainable solution for energy storage, making SIBs a focal point in battery research [1,2]. Due to the abundance of sodium resources, SIBs are more cost-effective than lithium-ion batteries (LIBs) and perform better under low-temperature conditions and in terms of safety [3,4]. Transition metal oxide cathodes with layered structures, such as $NaNi_{1/3}Fe_{1/3}Mn_{1/3}O_2$ (NFM), are promising due to their cost-effectiveness, environmental friendliness, and structural stability [5−7]. Despite the significant cost advantages of sodium-based layered oxide cathode materials, their large-scale application faces several limitations, including the following aspects. (1) Slow sodium-ion diffusion dynamics: compared to the radius of Li^+, the radius of Na^+ is larger (1.02 Å), leading to complex phase transitions during Na^+ extraction/insertion, which hinders Na^+ diffusion within the layers [8]. (2) Structural instability at high potential: When the potential exceeds 4 V, NFM undergoes an irreversible phase transition from *P*3 phase to *OP*2 phase, causing severe lattice distortion and a sharp decline in cycling performance, thus limiting its operating potential to below 4.0 V [9,10]. (3) Sodium/hydrogen exchange in moisture: Contact with atmospheric moisture leads to Na^+/H^+ exchange, causing Na^+ extraction from the bulk structure and forming alkaline

Corresponding author: Zhen-jiang HE, Tel: +86-15974290559, E-mail: hzjcsu@csu.edu.cn
https://doi.org/10.1016/S1003-6326(25)66940-8

impurities on the surface, which increases impedance and reduces SIB capacity [11−13].

Thus far, various modification techniques, including element doping, crystal structure modulation, and surface engineering, have been proposed to address the above bottlenecks [14−16]. Coating strategies effectively protect the electrode−electrolyte interface and reinforce the cathode against harmful side reactions [17]. However, single coating offers limited effectiveness in providing interfacial protection and does not directly enhance the overall structural stability of the cathode [18]. Ion doping at the transition metal (TM) sites within the O3-type layered cathode structure is widely explored to optimize Na^+ channels [19−21]. Thus, we proposed a bifunctional strategy that simultaneously achieved protective coating and ion doping, synergistically leveraging the benefits of both surface engineering techniques.

In this study, a ZrO_2 protective layer was constructed on the NFM surface via high-temperature calcination. Its impact on the structural stability and Na^+ diffusion dynamics was systematically explored. Various analytical techniques such as the X-ray diffraction (XRD), high-resolution transmission electron microscopy (HRTEM), and electrochemical performance tests were employed to characterize the effectiveness of the ZrO_2 modification. These results highlight the potential of this bifunctional strategy in improving the electrochemical performance and structural stability of SIB cathodes, offering a promising direction for future development of sodium-ion batteries.

2 Experimental

2.1 Synthesis procedure

Firstly, $Ni_{1/3}Fe_{1/3}Mn_{1/3}(OH)_2$ (HUAYOU New Energy Technology (Quzhou) Co., Ltd.) was mixed with Na_2CO_3 in a Na/Me (Me represents transition metal elements) stoichiometric ratio of 1.05∶1. The mixture was uniformly ground in an agate mortar. Subsequently, a tube furnace (KSL−1100x, Hefei Kejing Material Technologies Co., Ltd.) was used to sinter the mixture under air atmosphere. A two-stage sintering process was employed: 500 °C for 5 h in the first stage and 850 °C for 10 h in the second stage. After the sintering process, bare $NaNi_{1/3}Fe_{1/3}Mn_{1/3}O_2$ (NFM) particles were obtained. Next, nano-zirconia (1 wt.%) was mixed with the NFM particles in an automatic mixer for 1 h. This mixture was then heated in air at 600 °C for 10 h to obtain ZrO_2-coated NFM (ZrO_2@NFM). To further investigate the impact of the secondary calcination, an additional sample, NFM-resintering, was prepared by reheating the NFM sample at 600 °C for 10 h in air. This process was identical to the secondary calcination for the ZrO_2@NFM sample, but without ZrO_2 addition.

2.2 Characterization

Phase compositions and crystal structures were examined using XRD (Rigaku D/max−2500) at a scanning rate of 3 (°)/min over a range of 10°−80° using Cu K_α radiation. TEM (JEM−2100F) and SEM with energy-dispersive X-ray spectroscopy (SEM−EDS; JEOL JSM−6360LV, Japan) were used to study the morphology, microstructure, and distribution of elements in the prepared cathode. Valence states were studied using XPS (Thermo Fischer, ESCALAB 250Xi, USA) with a monochromatic Al K_α source.

2.3 Electrochemical measurements

CR2025 coin cells were assembled for electrochemical measurements. Firstly, the active material powder (NFM or ZrO_2@NFM, 80 wt.%), binder (PVDF, 10 wt.%), and conductive carbon (acetylene black, 10 wt.%) were mixed to form a slurry using N-methyl-2-pyrrolidone (NMP) as a solvent. This slurry was uniformly coated on Al foil and dried at 120 °C under vacuum for 12 h. The CR2025 cell comprised an NFM or ZrO_2@NFM cathode, counter electrode (sodium), and electrolyte. an EC/DMC solution with 1 mol/L $NaPF_6$ was used as the electrolyte. Cycle stability and rate performance were evaluated at 25 °C using a LAND (CT2001A) instrument from 2.0 to 4.0 V. CV and EIS tests were performed using a Princeton Applied Research potentiostat/galvanostat (VersaSTAT MC). EIS test was performed from 100 kHz to 0.01 Hz. Sodium-ion diffusion kinetics was examined by Galvanostatic Intermittent Titration Technique (GITT).

3 Results and discussion

3.1 Structural and morphological characteristics

The XRD patterns of NFM and ZrO_2@NFM (Fig. 1(a)) show the correspondence to $NaMn_{0.4}Fe_{0.2}Ni_{0.4}O_2$ ($R\bar{3}m$, No. 166). The sharpness and

definition of the diffraction peaks suggest that these samples have a high level of crystallinity. No impurity phases can be observed, suggesting that ions are successfully incorporated into the NFM lattice without disrupting its crystal structure. The (003) peak of ZrO_2@NFM is centered at a lower 2θ value than the (003) peak of bare NFM. This implies a larger d-spacing (the interplanar distance between adjacent (003) crystal planes) of the (003) peak. The d-spacing of the (003) peak is determined by both the TMO_2 layer (interplanar spacing) and the Na layer (interlayer spacing) [22]. This is consistent with the crystallographic data results obtained via Rietveld refinement (Table 1). Rietveld refined XRD patterns (Figs. 1(b, c)) confirm R_p (R_p is the profile R-factor) values of 3.03% and 1.71% for NFM and ZrO_2@NFM, respectively, with corresponding R_{wp} (R_{wp} is the weighted profile R-factor) values of 3.88% and 5.04%. This indicates that the refinement results are reliable and acceptable. The Na layer spacing of ZrO_2@NFM is broader than that of bare NFM (Table S1 in Supporting Information (SI)). This increased Na layer spacing might enhance the diffusion coefficients and rate capacity for Na^+ during charge−discharge cycling. Table 1 shows that the lattice parameters (a, b, c, and V) of ZrO_2@NFM are slightly smaller than those of NFM. Despite the larger atomic radius of Zr compared to those of the transition metal atoms and its stronger bonding with oxygen, the high-temperature calcination process used for coating ZrO_2 may induce compressive stress on the NFM lattice. This stress could lead to a slight reduction in the lattice parameters. To verify

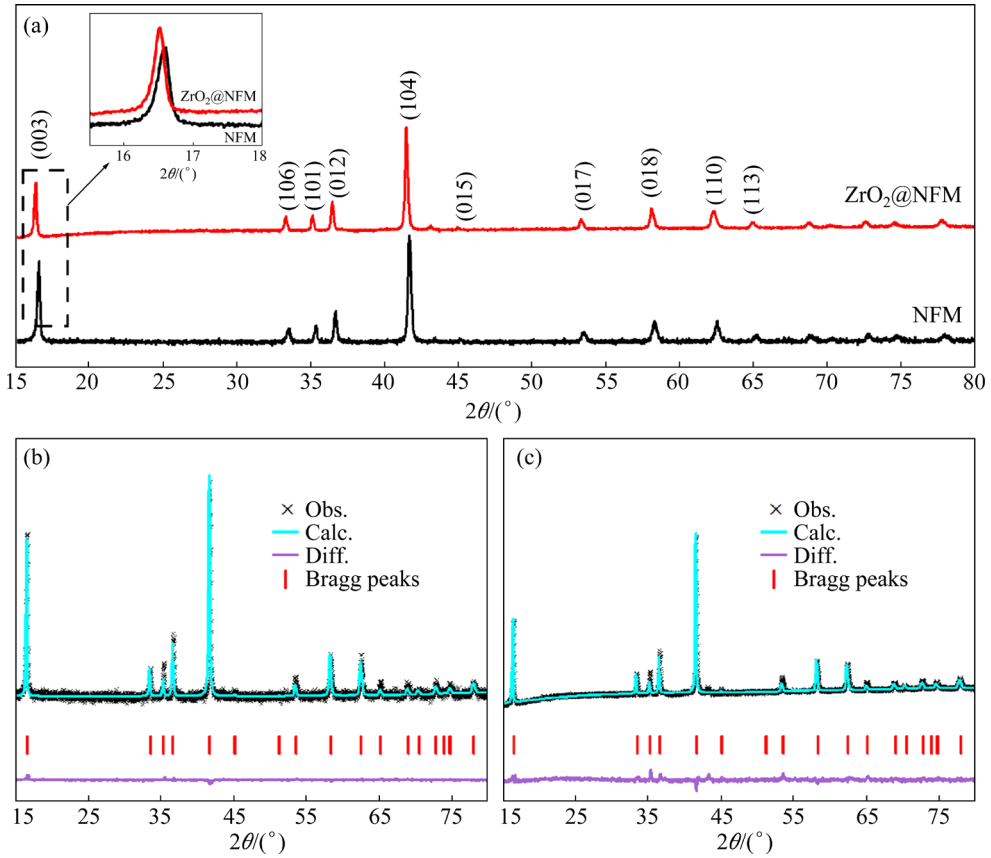

Fig. 1 XRD patterns and magnified (003) peak in 2θ range of 15.5°−18° of NFM and ZrO_2@NFM (a), Rietveld refinements of NFM (b) and ZrO_2@NFM (c)

Table 1 Rietveld refinement lattice parameters of NFM and ZrO_2@NFM

Sample	Lattice parameter			Volume, V/Å^3	Reliability factor	
	a/Å	b/Å	c/Å		R_p/%	R_{wp}/%
NFM	2.97624	2.97624	16.1114	123.594	3.03	3.88
ZrO_2@NFM	2.96894	2.96894	16.0119	122.229	1.71	5.04

this, we prepared a control sample, NFM-resintering, by reheating the NFM sample at 600 °C for 10 h without the addition of ZrO_2. The lattice parameters a, b, c, and V of NFM-resintering are also reduced compared to those of the original NFM sample, confirming that the lattice contraction is due to the secondary calcination process rather than the minor Zr^{4+} doping (Table S1 in SI).

The SEM images (Fig. S1 in SI) show that both NFM and ZrO_2@NFM consist of spherical agglomerates with particle sizes ranging from 6 to 8 μm, and an average primary particle size of about 100 nm. The surface of ZrO_2@NFM is rougher than that of NFM. EDS was performed to confirm the presence of Zr in ZrO_2@NFM. The obtained elemental maps (Figs. S1(d−i) in SI) indicate the uniform distribution of Na, Fe, Ni, Mn, and Zr across this sample.

High-resolution TEM (HR-TEM) micrographs of NFM and ZrO_2@NFM (Figs. 2(a, b)) show the grain edges with good crystallinity. These edges correspond to the (104) and (211) planes of the $R\bar{3}m$ space group. Moreover, a coating is clearly present on the surface of ZrO_2@NFM. Fast Fourier transform (FFT) patterns were employed to determine the crystal structures of different regions. Region 4, unlike Region 3 which is characterized by the $R\bar{3}m$ space group structure, is identified as a coating layer corresponding to the $P21/a$ (14) space group. Concurrently, Regions 1 and 2 are affirmed to conform to the $R\bar{3}m$ space group structure. This observation suggests that the NFM surface is partially covered by a ZrO_2 layer. EDS imaging was used to verify the coating (Figs. 2(c−j)). Zr is mostly found on the surface, further suggesting the existence of a ZrO_2 layer.

3.2 Valence state

The influence of Zr on the TM ion valence states in ZrO_2@NFM was evaluated by XPS (Fig. 3). The Ni 2p spectra (Figs. 3(a, b)) display two main peaks ascribed to Ni $2p_{3/2}$ and Ni $2p_{1/2}$, with additional satellite peaks observed on the left side. Deconvoluted Ni $2p_{3/2}$ peaks are observed at approximately 854.1 eV (Ni^{2+}) and 856.1 eV (Ni^{3+}). Deconvolution of the Ni $2p_{1/2}$ peak provides peaks at 872.1 eV (Ni^{2+}) and 875.9 eV (Ni^{3+}). The Fe 2p spectra (Figs. 3(c, d)) show peaks at 710.4 eV (Fe $2p_{3/2}$) and 724.6 eV (Fe $2p_{1/2}$), confirming the existence of Fe^{3+}. The smaller peaks are satellite peaks. The Mn 2p spectra (Figs. 3(e, f)) display Mn^{3+} peaks at about 642.2 eV (Mn $2p_{3/2}$) and 653.3 eV (Mn $2p_{1/2}$). Mn^{4+} peaks can also be observed at 644.6 eV (Mn $2p_{3/2}$) and 655.5 eV (Mn $2p_{1/2}$) [23,24]. The content of Mn^{3+} in the NFM sample is much greater than that in the ZrO_2@NFM sample,

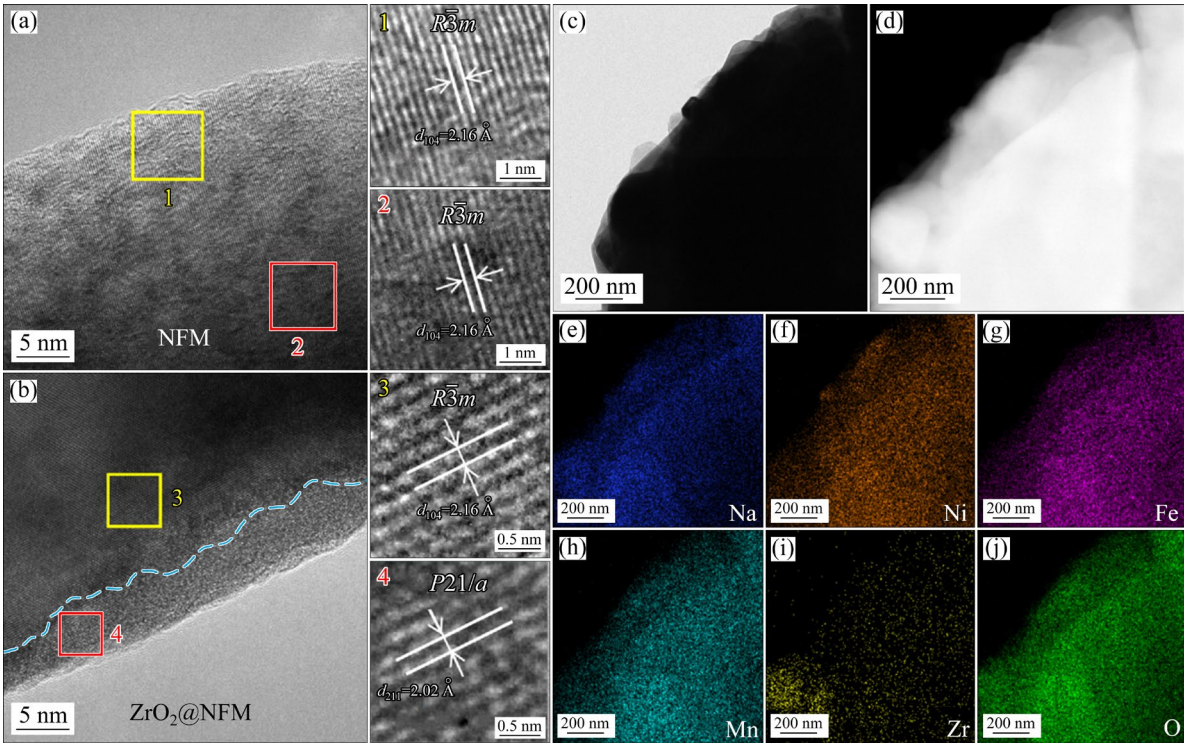

Fig. 2 HR-TEM images of NFM (a) and ZrO_2@NFM (b), and EDS mappings of ZrO_2@NFM (c−j)

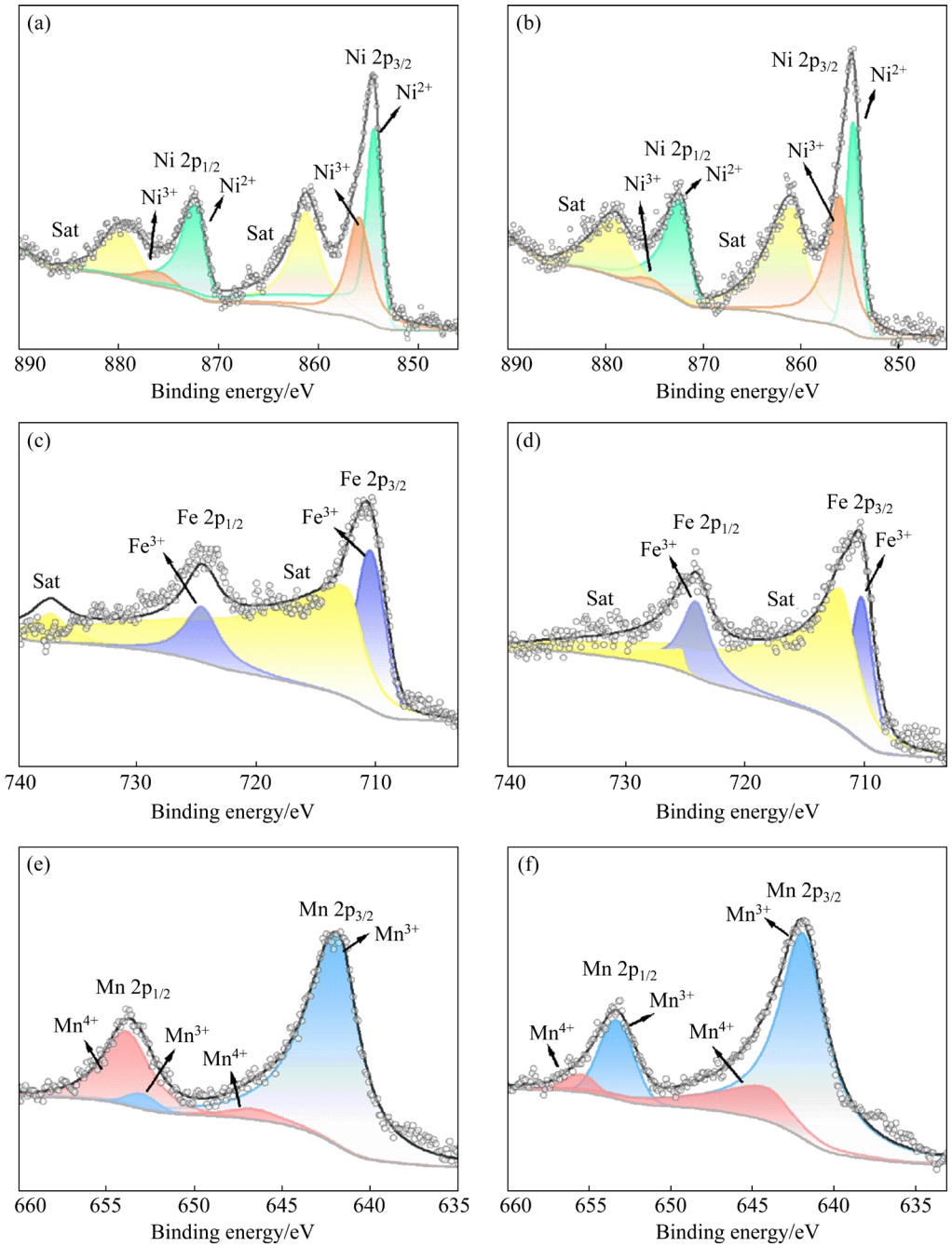

Fig. 3 XPS spectra and fitting results of NFM (a, c, e) and ZrO_2@NFM (b, d, f): (a, b) Ni 2p; (c, d) Fe 2p; (e, f) Mn 2p

indicating that the ZrO_2 coating mainly affects the Mn^{3+}/Mn^{4+} ratio. Mn^{3+} acts as a Jahn−Teller active ion, causing a Jahn−Teller effect that results in permanent alterations to the material structure. Therefore, high Mn^{3+} content may lead to structural instability [25,26].

3.3 Electrochemical performance

The rate capability and charge−discharge curves of both cathodes at various current densities are displayed in Figs. 4(a, c, d). ZrO_2@NFM shows superior rate capability compared to NFM (Fig. 4(a)). This is due to the protective role of the ZrO_2 layer, which inhibits surface side reactions. The bare NFM has discharge capacities of 117.2 mA·h/g (0.2*C*), 109.3 mA·h/g (0.5*C*), 105.4 mA·h/g (1*C*), 99.2 mA·h/g (2*C*), and 84.5 mA·h/g (5*C*) (Fig. 4(c)). In contrast, ZrO_2@NFM shows notably improved discharge capacities of 131 mA·h/g (0.2*C*), 124.3 mA·h/g (0.5*C*), 119.8 mA·h/g (1*C*), 113.5 mA·h/g (2*C*), and 100 mA·h/g (5*C*) (Fig. 4(d)). The enhanced capacity of ZrO_2-modified samples at lower rates (e.g., 0.2*C*) can be attributed to the oxygen redox

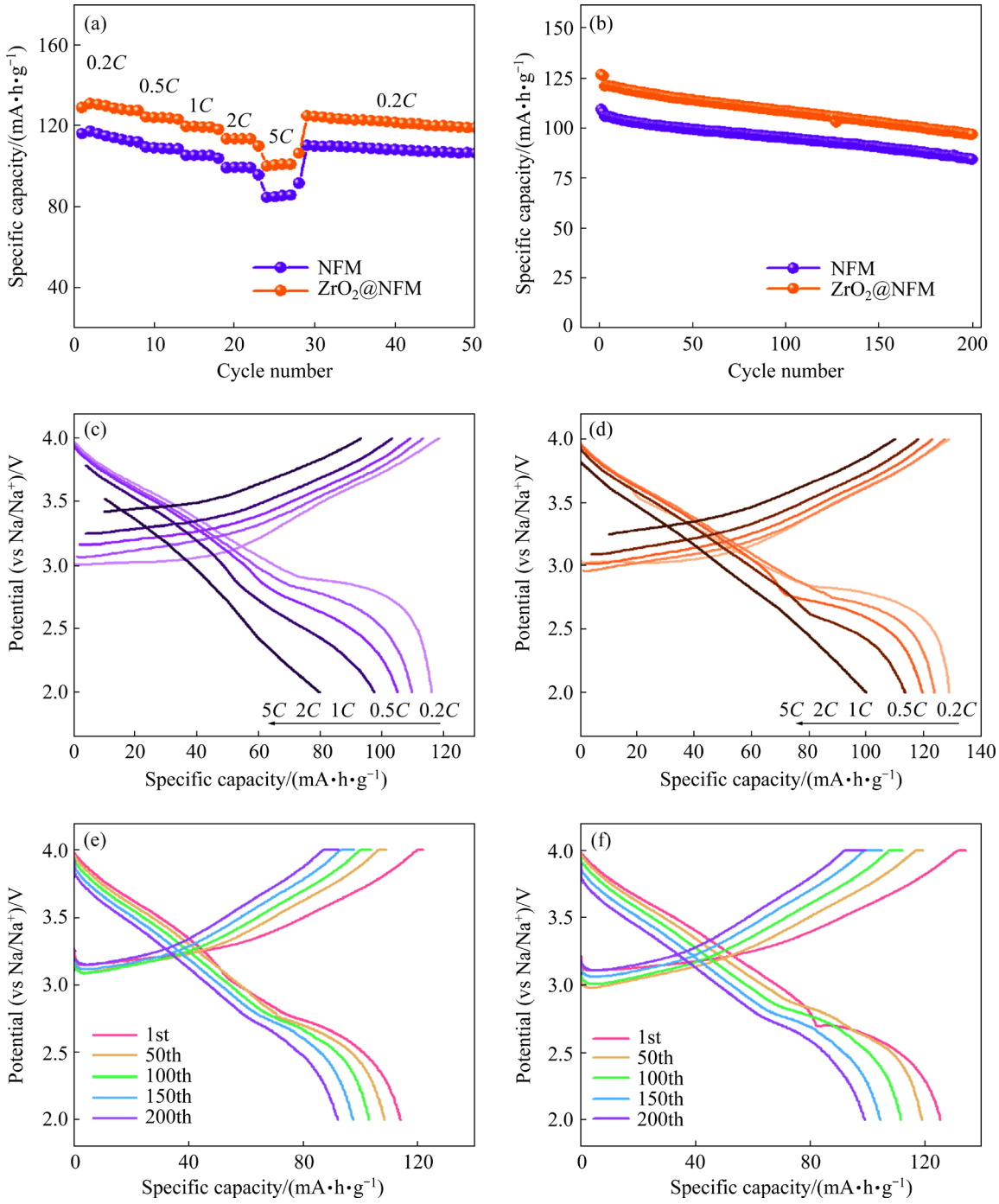

Fig. 4 Rate capability of NFM and ZrO_2@NFM (a); Charge−discharge curves of NFM (c) and ZrO_2@NFM (d) at different rates; Cycling performance of NFM and ZrO_2@NFM at 1*C* for 200 cycles (b), and corresponding charge−discharge plots of NFM (e) and ZrO_2@NFM (f) (All curves obtained in potential range of 2.0−4.0 V)

capability of the NFM material. The high bond energy of Zr—O compared to TM—O bonds (Zr—O: 760 kJ/mol; Ni—O: 391.6 kJ/mol; Fe—O: 409 kJ/mol; Mn—O: 402 kJ/mol) promotes reversible oxygen redox reactions [27]. This is evidenced by the XPS results shown in Fig. S2 in SI, where the ZrO_2@NFM sample exhibits a stronger O^{n-} peak compared to NFM. Consequently, the partial Zr doping in the modified sample contributes to a small amount of reversible lattice oxygen redox capacity, leading to higher capacities across different rates [28,29]. Additionally, the structural adjustments in ZrO_2@NFM, including the decrease in Na—O and O—O bond lengths, along with the

increase in TM—O bond lengths (Table S1 in SI), result in a more compact structural arrangement. This compactness enhances the migration and diffusion capacity of Na^+ during charge−discharge process by reducing electrostatic repulsion between Na^+ and O^{2-}, thereby improving electrochemical performance [30,31]. After 200 cycles at 1*C*, the capacity retentions of NFM and ZrO_2@NFM are 79.81% and 80.16%, respectively (Figs. 4(b, e, f)). ZrO_2@NFM continuously maintains high specific capacities and good capacity retention because it has an enhanced Na^+ diffusion coefficient.

The CV curves of NFM and ZrO_2@NFM were obtained at 2.0−4.0 V (Figs. 5(a, b, d)). The high-potential range has two sets of redox peaks that correspond to the sloping region in the charge−discharge curves, indicating that the electrode is sodium-poor. The plateau in the low-potential region of the charge−discharge curves indicates that the electrode materials are in a sodium-rich state [32]. During charging, the bare NFM cathode shows oxidation peaks at 3.75 and 3.45 V that are potentially ascribed to the successive oxidation reactions of Fe^{3+}/Fe^{4+} and Ni^{2+}/Ni^{4+} (including Ni^{2+}/Ni^{3+} and Ni^{3+}/Ni^{4+}), respectively [33,34]. There are three corresponding reduction peaks during battery discharge related to Fe^{4+}/Fe^{3+} reduction at 3.58 V, Ni^{4+}/Ni^{3+} reduction at 2.76 V, and Ni^{3+}/Ni^{2+} reduction at 2.41 V. The primary oxidation peaks of the ZrO_2@NFM cathode are present at 3.75 and 3.41 V, and the three corresponding reduction peaks are observed at 3.58, 2.89, and 2.67 V. The potential difference of the redox peaks of NFM is $\Delta\varphi_{Ni}$= 1.04 V and that of ZrO_2@NFM is $\Delta\varphi_{Ni}$=0.74 V. Therefore, the ZrO_2@NFM cathode exhibits significantly lower polarization, leading to better reversibility during the charging and discharging processes. These improvements will help to increase its cycle performance. Furthermore, the ZrO_2@NFM cathode displays a stronger current response compared to NFM, confirming that coating the cathode material with ZrO_2 improves the reaction kinetics.

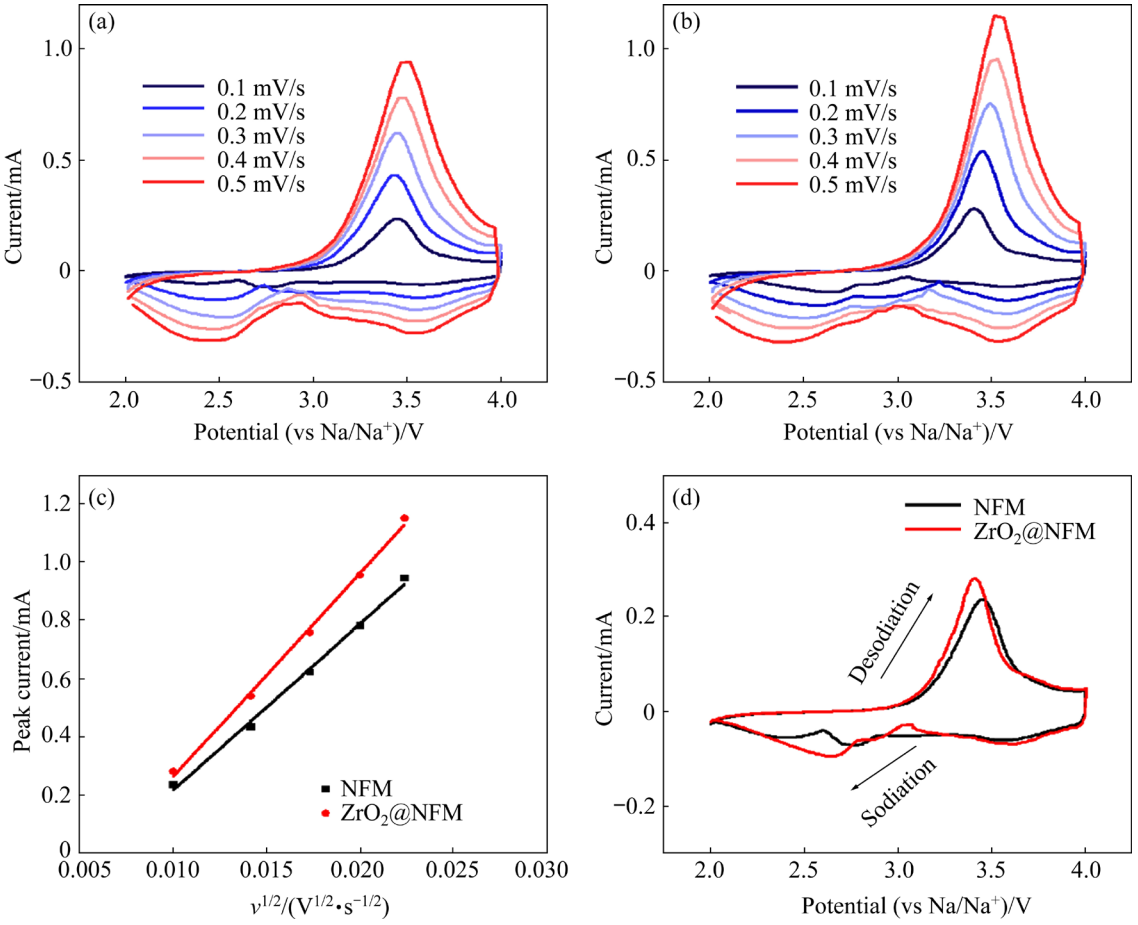

Fig. 5 CV curves of NFM (a) and ZrO_2@NFM (b) at scanning rates of 0.1−0.5 mV/s in potential range of 2−4 V, peak current versus scanning rate $v^{1/2}$ (c), and CV curves of samples at scanning rate of 0.1 mV/s in potential range of 2−4 V (d)

3.4 Diffusion kinetics and impedance

The CV curves of ZrO_2@NFM and NFM were obtained at varying scanning rates (v) (0.1−0.5 mV/s, Figs. 5(a, b, c) to study the Na^+ diffusion kinetics in each electrode. With increasing scanning rate, the peak current (I_p) rises, the reduction peaks shift in the lower-potential direction, and the oxidation peaks shift in the higher-potential direction. Formula (1) was used to calculate the solid-state Na^+ diffusion rate, which governs Na^+ transfer throughout the cycle process.

$$I_p=2.69\times10^5 n^{3/2} A D_{Na^+}^{1/2} v^{1/2} \Delta C_0 \quad (1)$$

where n, A, D_{Na^+}, and ΔC_0 represent the number of transported electrons in a single reaction, electrode area, Na^+ diffusion coefficient, and the change in concentration of Na^+ during the electrochemical reaction process, respectively. $v^{1/2}$ and I_p are linearly related. The Na^+ diffusion coefficient values were computed by linearly fitting the slopes of peak currents at various scanning rates (Fig. 5(c)). ZrO_2@NFM has a higher average Na^+ diffusion coefficient (10.5948×10^{-11} cm^2/s) compared to NFM (7.09104×10^{-11} cm^2/s), as shown in Table 2. Thus, ZrO_2 modification significantly enhances the Na^+ diffusion kinetics of NFM.

Table 2 Apparent Na^+ diffusion coefficients (D_{Na^+}) during charging process obtained by CV

Sample	Slope	D_{Na^+}/(10^{-11}cm^2·s^{-1})
NFM	0.05721	7.09104
ZrO_2@NFM	0.06993	10.5948

To further study the electrochemical behavior related to phase transition during long-term cycling from 2.0 to 4.0 V, differential charge/discharge capacity (Q) tests were performed (Fig. 6). Visible oxidation peaks can be identified as the $O3$ to $P3$ phase transition [35,36]. Compared to NFM, the peaks of ZrO_2@NFM are located at lower potentials, suggesting a quicker transition to the $P3$ phase during

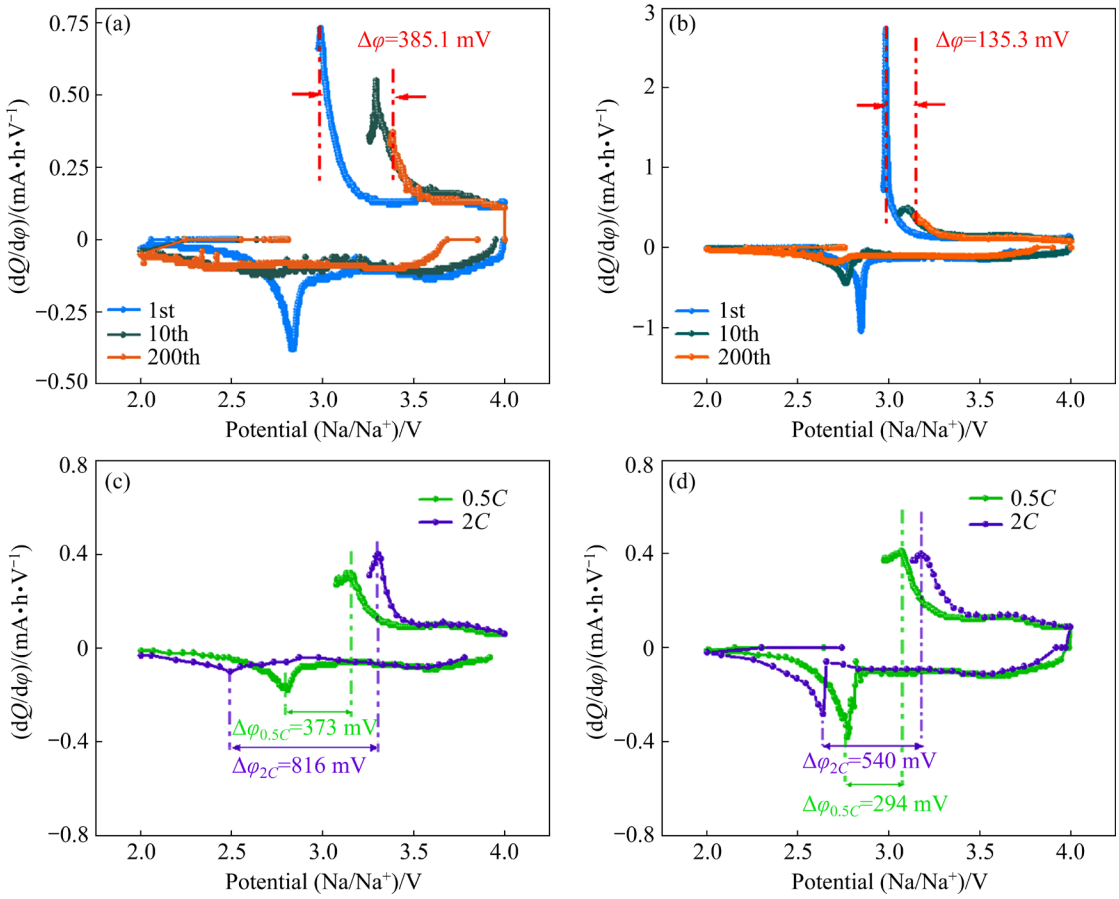

Fig. 6 Differential charge/discharge capacity profiles (dQ/dφ) of NFM (a, c) and ZrO_2@NFM (b, d): (a, b) Cycle-dependent dQ/dφ curves for 1st, 10th, and 200th cycles; (c, d) Rate-dependent dQ/dφ curves at various current densities of 0.5C and 2C

the sodium desorption process. The diffusion of Na^+ in the *O*3 phase occurs via intermediary tetrahedral sites (from octahedral sites to neighboring octahedral sites). Na^+ transfer creates a prismatic site in the *P*3 phase and proceeds straight to a face-sharing prismatic site. This transition lowers the transfer energy barrier [37]. Consequently, the early presence of the *P*3 phase may aid in quick ionic transfer, leading to the improved rate capacity [38,39]. The peak oxidation potentials ($\Delta\varphi$) of fresh ZrO_2@NFM and NFM cathodes and the same cathodes after 200 cycles were determined at 1*C*. For both samples, the peak shifts to a higher potential after cycling. NFM experiences severe polarization, as indicated by its considerable peak shift ($\Delta\varphi$=385.1 mV) and noticeable drop in peak intensity. In contrast, ZrO_2@NFM shows a remarkably small peak shift ($\Delta\varphi$=135.3 mV), suggesting a much lower degree of polarization compared to NFM. This implies that the Zr doping-coating approach reduces the polarization and increases the structural stability.

EIS impedance tests were performed and Na^+ diffusion coefficients were calculated to study the influence of ZrO_2 on the Na^+ diffusion kinetics of NFM and ZrO_2@NFM. Nyquist plots (Figs. 7(a, b)) display a semicircle (at high frequencies, associated with interfacial charge transfer resistance R_{ct}) and

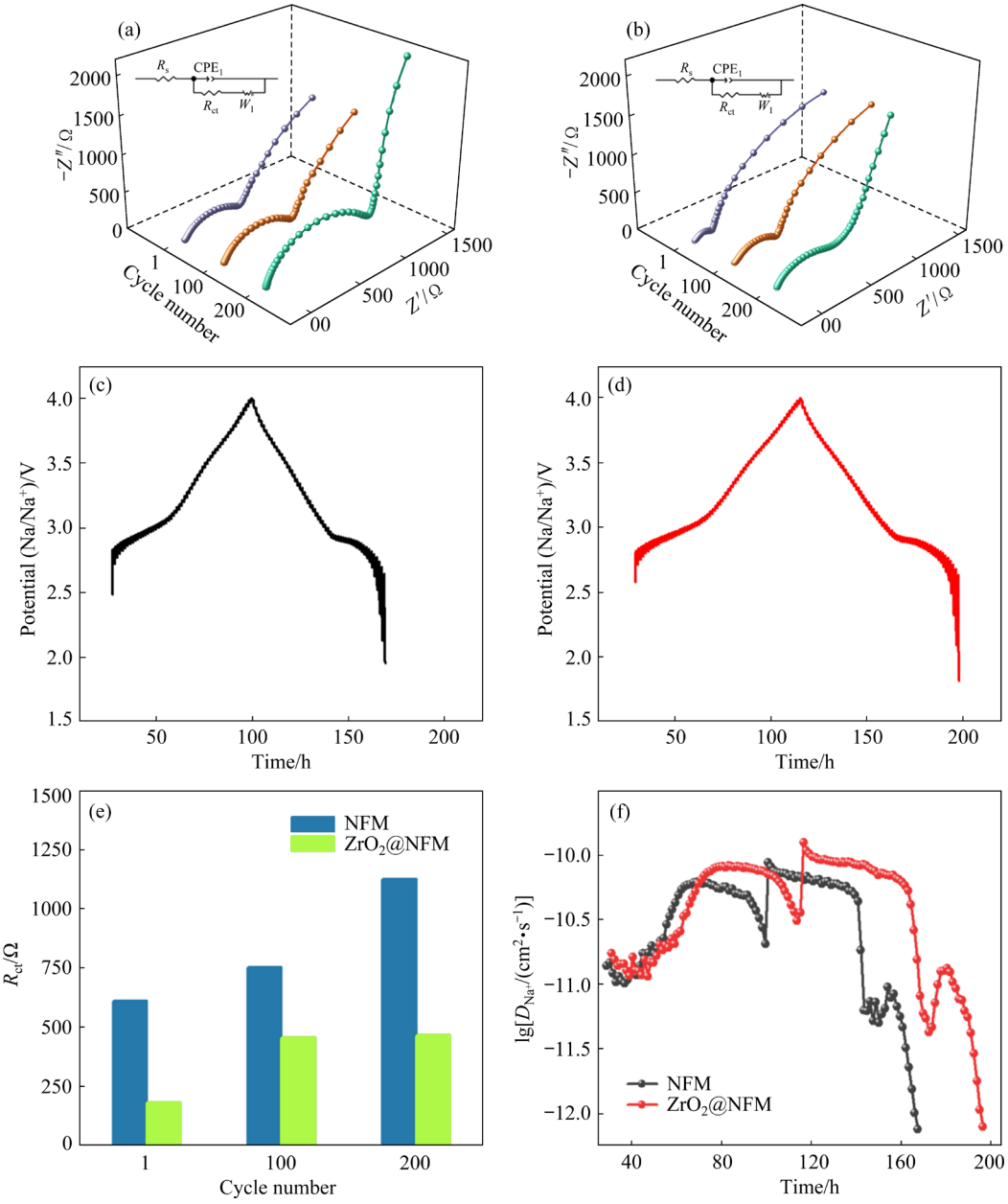

Fig. 7 Nyquist plots and equivalent circuits (in insets) of NFM (a) and ZrO_2@NFM (b), GITT profiles of NFM (c) and ZrO_2@NFM (d), EIS fitting results of samples (e), and D_{Na^+} values during charge−discharge process (f)

straight line (at low frequencies, associated with Warburg impedance Z_w) [40]. EIS analysis results show that after 200 cycles, the R_{ct} value of ZrO_2@NFM (465.4 Ω) is significantly lower than that of NFM (1125 Ω). The lower R_{ct} caused by the ZrO_2 coating inhibits unfavorable responses on the surface. Furthermore, the low conductivity of the ZrO_2 coating has no effect on the resistance of the cathode because it is only 2−5 nm in thickness.

GITT was employed to validate the cathodes at various potentials throughout the charge and discharge phases. Typical charging−discharging GITT curves are shown in Figs. 7(c, d). After one cycle at 0.1*C*, a current pulse of 20 min was applied at the same current density, followed by a 60 min relaxation to achieve potential equilibrium. The Na^+ diffusion coefficients D_{Na^+} were calculated, as displayed in Fig. 7(f). The D_{Na^+} values of the ZrO_2@NFM cathode are significantly improved compared to that of the NFM cathode. The higher Na^+ diffusion coefficient and lower electrochemical polarization of ZrO_2@NFM are due to the expanded Na^+ transport routes.

4 Conclusions

(1) The NFM cathode material was successfully coated with ZrO_2 and doped with Zr^{4+}. The ZrO_2 coating inhibited the surface side reactions and reduced the electrode polarization.

(2) Doping Zr^{4+} into the TM layer resulted in shorter O—O and TM—O bonds, stabilizing the layered structure. Additionally, the ZrO_2 modification widened the Na layer spacing and lowered the migration barrier.

(3) Compared to uncoated NFM, ZrO_2@NFM exhibited a reduced Mn^{3+} content, which helped to inhibit the Jahn−Teller phenomenon.

(4) The ZrO_2 surface engineering significantly enhanced the Na^+ diffusion kinetics. The modified electrode demonstrated improved rate performance and cycling stability.

CRediT authorship contribution statement

Wei-jia TANG: Investigation, Writing − Original draft, Data curation, Visualization; **Yun-jiao LI:** Supervision, Project administration, Resources; **Yu-ming LIU:** Methodology, Investigation; **Chang-long LEI:** Investigation, Validation; **Shi-jie JIANG:** Conceptualization, Data curation; **Zhen-jiang HE:** Project administration, Writing − Review & editing, Funding acquisition.

Declaration of competing interest

The authors declare that they have no known competing financial interests or personal relationships that could have appeared to influence the work reported in this paper.

Acknowledgments

This work was supported by the Central South University Innovation-Driven Research Programme, China (No. 2023CXQD053), the National Natural Science Foundation of China (No. 52274310), and financial support from the Government of Chongzuo, Guangxi Zhuang Autonomous Region, China (No. FA20210713).

Supporting Information

Supporting Information in this paper can be found at: https://tnmsc.csu.edu.cn/download/17-p4230-2024-0422-Supporting_Information.pdf.

References

[1] CHANG Yi-jiao, XIE Guang-hui, ZHOU Yong-mao, WANG Jie-xi, WANG Zhi-xing, GUO Hua-jun, YOU Bian-zheng, YAN Guo-chun. Enhancing storage performance of P2-type $Na_{2/3}Fe_{1/2}Mn_{1/2}O_2$ cathode materials by Al_2O_3 coating [J]. Transactions of Nonferrous Metals Society of China, 2022, 32(1): 262−272.

[2] PENG Bo, WAN Guang-lin, AHMAD N, YU Lai, MA Xin-yi, ZHANG Gen-qiang. Recent progress in the emerging modification strategies for layered oxide cathodes toward practicable sodium ion batteries [J]. Advanced Energy Materials, 2023, 13(27): 2300334.

[3] GUO Yu-jie, JIN Ruo-xi, FAN Min, WANG Wen-peng, XIN Sen, WAN Li-jun, GUO Yu-guo. Sodium layered oxide cathodes: Properties, practicality and prospects [J]. Chemical Society Reviews, 2024, 53(15): 7828−7874.

[4] CAO Yuan-lin YANG Xiu-kang, WANG Lu, XIAO Ling, FU Ni ZOU Li, MA Wen-bo LIU Zhe-ting, WANG Xiao-qin, LIU Li, SHU Hong-bo, WANG Xian-you. Improving electrochemical performance of Ni-rich layered oxide cathodes via one-step dual modification strategy [J]. Transactions of Nonferrous Metals Society of China, 2022, 32(11): 3663−3678.

[5] HUANG Qun, WANG Mei-yu, ZHANG Li, QI Shuo, FENG Yi-ming, HE Ping-ge, JI Xiao-bo, WANG Peng, ZHOU Liang-jun, CHEN Shuang-qiang, WEI Wei-feng. Shear-resistant interface of layered oxide cathodes for sodium ion batteries [J]. Energy Storage Materials, 2022, 45: 389−398.

[6] WANG Qing, MARIYAPPAN S, ROUSSE G, MOROZOV A V, PORCHERON B, DEDRYVÈRE R, WU Jin-peng, YANG Wan-li, ZHANG Lei-ting, CHAKIR M, AVDEEV M, DESCHAMPS M, YU Y S, CABANA J, DOUBLET M L,

ABAKUMOV A M, TARASCON J M. Unlocking anionic redox activity in O3-type sodium 3d layered oxides via Li substitution [J]. Nature Materials, 2021, 20(3): 353−361.

[7] ZUO Wen-hua, INNOCENTI A, ZARRABEITIA M, BRESSER D, YANG Yong, PASSERINI S. Layered oxide cathodes for sodium-ion batteries: Storage mechanism, electrochemistry, and techno-economics [J]. Accounts of Chemical Research, 2023, 56(3): 284−296.

[8] ZHAO Yan-shuo, LIU Qi, ZHAO Xiao-han, MU Dao-bin, TAN Guo-qiang, LI Li, CHEN Ren-jie, WU Feng. Structure evolution of layered transition metal oxide cathode materials for Na-ion batteries: Issues, mechanism and strategies [J]. Materials Today, 2023, 62: 271−295.

[9] CHEN Tao, OUYANG Bai-xue, FAN Xiao-wen, ZHOU Wei-li, LIU Wei-fang, LIU Kai-yu. Oxide cathodes for sodium-ion batteries: Designs, challenges, and perspectives [J]. Carbon Energy, 2022, 4(2): 170−199.

[10] MU Lin-qin, RAHMAN M M, ZHANG Yan, FENG Xu, DU Xi-wen, NORDLUND D, LIN Feng. Surface transformation by a “cocktail” solvent enables stable cathode materials for sodium ion batteries [J]. Journal of Materials Chemistry A, 2018, 6(6): 2758−2766.

[11] YAO Hu-rong, ZHENG Li-tuo, XIN Sen, GUO Yu-guo. Air-stability of sodium-based layered-oxide cathode materials [J]. Science China Chemistry, 2022, 65(6): 1076−1087.

[12] SUN Y K. Direction for commercialization of O3-type layered cathodes for sodium-ion batteries [J]. ACS Energy Letters, 2020, 5(4): 1278−1280.

[13] LIU Yi-feng, HAN Kai, PENG Dan-ni, KONG Ling-yi, SU Yu, LI Hong-wei, HU Hai-yan, LI Jia-yang, WANG Hong-rui, FU Zhi-qiang, MA Qiang, ZHU Yan-fang, TANG Rui-ren, CHOU Shu-lei, XIAO Yao, WU Xiong-wei. Layered oxide cathodes for sodium-ion batteries: From air stability, interface chemistry to phase transition [J]. InfoMat, 2023, 5(6): e12422.

[14] HONG Ning-yun, LI Jian-wei, GUO Shi-hong, HAN Hua-wei, WANG Hao-ji, HU Xin-yu, HUANG Jiang-nan, ZHANG Bai-chao, HUA Fang, SONG Bai, BUGDAY N, YASAR S, ALTIN S, DENG Wen-tao, ZOU Guo-qiang, HOU Hong-shuai, LONG Zhen, JI Xiao-bo. An in situ dual-modification strategy for O3-$NaNi_{1/3}Fe_{1/3}Mn_{1/3}O_2$ towards high-performance sodium-ion batteries [J]. Journal of Materials Chemistry A, 2023, 11(35): 18872−18880.

[15] JO J H, CHOI J U, KONAROV A, YASHIRO H, YUAN S, SHI L Y, SUN Y Y, MYUNG S T. Sodium-ion batteries: Building effective layered cathode materials with long-term cycling by modifying the surface via sodium phosphate [J]. Advanced Functional Materials, 2018, 28(14): 1705968.

[16] JI Hao-cheng, ZHAI Jing-jun, CHEN Guo-jie, QIU Xiao, FANG Hui, ZHANG Tao-lüe, HUANG Zhong-yuan, ZHAO Wen-guang, WANG Zhen-hui, CHU Mi-hai, WANG Rui, WANG Chao-qi, LI Rui, ZENG Wen, WANG Xin-wei, XIAO Yin-guo. Surface engineering suppresses the failure of biphasic sodium layered cathode for high performance sodium-ion batteries [J]. Advanced Functional Materials, 2022, 32(12): 2109319.

[17] MU Lin-qin, FENG Xu, KOU Rong-hui, ZHANG Yan, GUO Hao, TIAN Chi-xia, SUN Cheng-jun, DU Xi-wen, NORDLUND D, XIN Huo-lin, LIN Feng. Deciphering the cathode−electrolyte interfacial chemistry in sodium layered cathode materials [J]. Advanced Energy Materials, 2018, 8(34): 1801975.

[18] LI Hai-ming, WANG Tai-lin, WANG Xue, LI Guang-da, DU Yi, SHEN Jian-xing, CHAI Jin-ling. Sodium superionic conductor $NaTi_2(PO_4)_3$ surface layer modified P2-type $Na_{2/3}Ni_{1/3}Mn_{2/3}O_2$ as high-performance cathode for sodium-ion batteries [J]. Journal of Power Sources, 2021, 494: 229771.

[19] CHENG Lei, ZHAO Yi, HUANG Bin, ZHAO Zao-wen, LI Yan-wen, LI Wei. Effects of W-doping on precursor growth of $LiNi_{0.88}Co_{0.09}Mn_{0.03}O_2$ and its electrochemical performance [J]. Transactions of Nonferrous Metals Society of China, 2024, 34(4): 1251−1262.

[20] YU T Y, HWANG J Y, BAE I T, JUNG H G, SUN Y K. High-performance Ti-doped O3-type $NaTi_x(Ni_{0.6}Co_{0.2}Mn_{0.2})_{1-x}O_2$ cathodes for practical sodium-ion batteries [J]. Journal of Power Sources, 2019, 422: 1−8.

[21] TAN Lei, WU Qi-feng, LIU Zeng-sheng, CHEN Qi-heng, YI Hong-ling, ZHAO Zi-xiang, SONG Liu-bin, ZHONG Sheng-kui, WU Xian-wen, LI Ling-jun. Ti-substituted O3-type layered oxide cathode material with high-voltage stability for sodium-ion batteries [J]. Journal of Colloid and Interface Science, 2022, 622: 1037−1044.

[22] SHIN J W, SON J T. Novel core-shell-type design of $Na_{0.5}[Li_{0.5}(Ni_{0.8}Co_{0.1}Mn_{0.1})_{1-x}(Ni_{0.5}Co_{0.1}Mn_{0.4})_x]O_2$ cathode material for sodium-ion batteries [J]. Journal of Nanoscience and Nanotechnology, 2019, 19(3): 1335−1339

[23] ZHENG Li-tuo, LI Ling-jun, SHUNMUGASUNDARAM R, OBROVAC M N. Effect of controlled-atmosphere storage and ethanol rinsing on $NaNi_{0.5}Mn_{0.5}O_2$ for sodium-ion batteries [J]. ACS Applied Materials & Interfaces, 2018, 10(44): 38246−38254.

[24] PU Xiang-jun, WANG Hui-ming, ZHAO Dong, YANG Han-xi, AI Xin-ping, CAO Shu-nan, CHEN Zhong-xue, CAO Yu-liang. Recent progress in rechargeable sodium-ion batteries: Toward high-power applications [J]. Small, 2019, 15(32): e1805427.

[25] CHE Hai-ying, YANG Xin-rong, YU Yan, PAN Chao-liang, WANG Hong, DENG Yong-hong, LI Lin-sen, MA Zi-feng. Engineering optimization approach of nonaqueous electrolyte for sodium ion battery with long cycle life and safety [J]. Green Energy & Environment, 2021, 6(2): 212−219.

[26] WANG Peng-fei, YAO Hu-rong, LIU Xin-yu, ZHANG Jie-nan, GU Lin, YU Xi-qian, YIN Ya-xia, GUO Yu-guo. Ti-substituted $NaNi_{0.5}Mn_{0.5-x}Ti_xO_2$ cathodes with reversible O3−P3 phase transition for high-performance sodium-ion batteries [J]. Advanced Materials, 2017, 29(19): 1700210.

[27] KIM S, MIN K, PARK K. Y-doped P2-type $Na_{0.67}Ni_{0.33}Mn_{0.67}O_2$: A sodium-ion battery cathode with fast charging and enhanced cyclic performance [J]. Journal of Alloys and Compounds, 2021, 874: 160027.

[28] WANG Guan, XIE Cheng-hao, WANG Hong, LI Quan, XIA Fan-jie, ZENG Wei-hao, PENG Hao-yang, van TENDELOO G, TAN Gang-jian, TIAN Jin-sai, WU Jin-song. Mitigated oxygen loss in lithium-rich manganese-based cathode enabled by strong Zr−O affinity [J]. Advanced Functional Materials, 2024, 34(23): 2313672.

[29] REN Hai-xia, ZHENG Lu-min, LI Yu, NI Qiao, QIAN Ji, LI Ying, LI Qiao-jun, LIU Ming-quan, BAI Ying, WENG Su-ting, WANG Xue-feng, WU Feng, WU Chuan. Impurity-vibrational entropy enables quasi-zero-strain layered oxide cathodes for high-voltage sodium-ion batteries [J]. Nano Energy, 2022, 103: 107765.

[30] HWANG J Y, MYUNG S T, CHOI J U, YOON C S, YASHIRO H, SUN Y K. Correction: Resolving the degradation pathways of the O3-type layered oxide cathode surface through the nano-scale aluminum oxide coating for high-energy density sodium-ion batteries [J]. Journal of Materials Chemistry A, 2018, 6(8): 3754.

[31] MENG Xiang-cong, LIANG Jin-ji, LIANG Min, LI Wen-ya, LIN Chen-han, KE Xi, SHI Zhi-cong, LIU Li-ying. Superior rate performance and structural evolution of O3-type layered $NaCrO_2$ for sodium ion batteries at high temperatures [J]. Science China: Materials, 2023, 66(9): 3445−3452.

[32] WANG Xian-zuo, ZUO Yu-ting, QIN Yuan-bin, ZHU Xu, XU Shao-wen, GUO Yu-jie, YAN Tian-ran, ZHANG Liang, GAO Zhi-bin, YU Lian-zheng, LIU Meng-ting, YIN Ya-xia, CHENG Yong-hong, WANG Peng-fei, GUO Yu-guo. Fast Na^+ kinetics and suppressed voltage hysteresis enabled by a high-entropy strategy for sodium oxide cathodes [J]. Advanced Materials, 2024, 36(24): e2312300.

[33] SHEVCHENKO V A, GLAZKOVA I S, NOVICHKOV D A, SKVORTSOVA I, SOBOLEV A V, ABAKUMOV A M, PRESNIAKOV I A, DROZHZHIN O A, ANTIPOV E V. Competition between the Ni and Fe redox in the O3-$NaNi_{1/3}Fe_{1/3}Mn_{1/3}O_2$ cathode material for Na-ion batteries [J]. Chemistry of Materials, 2023, 35(10): 4015−4025.

[34] SUN Li-qi, XIE Ying-ying, LIAO Xiao-Zhen, WANG Hong, TAN Guo-qiang, CHEN Zong-hai, REN Yang, GIM J, TANG Wan, HE Yu-shi, AMINE K, MA Zi-feng. Insight into Ca-substitution effects on O3-type $NaNi_{1/3}Fe_{1/3}Mn_{1/3}O_2$ cathode materials for sodium-ion batteries application [J]. Small, 2018, 14(21): 1704523.

[35] LIN Chun-gang, DAI Peng, WANG Xiao-lin, SUN Jing-jing, ZHUANG Shu-xin, WU Li-na, LU Mi, WEN Yan-fen. P2/O3 biphase integration promoting the enhancement of structural stability for sodium layered oxide cathode [J]. Chemical Engineering Journal, 2024, 480: 147964.

[36] JEONG M, LEE H, YOON J, YOON W. O3-type $NaNi_{1/3}Fe_{1/3}Mn_{1/3}O_2$ layered cathode for Na-ion batteries: Structural evolution and redox mechanism upon Na (de) intercalation [J]. Journal of Power Sources, 2019, 439: 227064.

[37] WU Lin-rong, ZHANG Yu-han, WU Zhen, TIAN Jin-lü, WANG Hao-rui, ZHAO Hai-jun, XU Shou-dong, CHEN Liang, DUAN Xiao-chuan, ZHANG Ding, GUO Hui-juan, YOU Ya, ZHU Zhi. Stabilized O3-type layered sodium oxides with enhanced rate performance and cycling stability by dual-site Ti^{4+}/K^+ substitution [J]. Advanced Science, 2023, 10(32): e2304067.

[38] DAI Li-ling, GUO Zi-yin, WANG Zhao, XU Shun-jie, WANG Shui-long, LI Wen-lu, ZHANG Guo-dong, CHENG Ya-jun, XIA Yong-gao. Defensive and ion conductive surface layer enables high rate and durable O3-type $NaNi_{1/3}Fe_{1/3}Mn_{1/3}O_2$ sodium-ion battery cathode [J]. Small, 2024, 20(2): 2305019.

[39] YU Yang, NING De, LI Qing-yuan, FRANZ A, ZHENG Li-rong, ZHANG Nian, REN Guo-xi, SCHUMACHER G, LIU Xiang-feng. Revealing the anionic redox chemistry in O3-type layered oxide cathode for sodium-ion batteries [J]. Energy Storage Materials, 2021, 38: 130−140.

[40] QI Xing-guo, LIU Li-lu, SONG Ning-ning, GAO Fei, YANG Kai, LU Ya-xiang, YANG Hai-tao, HU Yong-sheng, CHENG Zhao-hua, CHEN Li-quan. Design and comparative study of O3/P2 hybrid structures for room temperature sodium-ion batteries [J]. ACS Applied Materials & Interfaces, 2017, 9(46): 40215−40223.

氧化锆涂层对钠离子电池 $NaNi_{1/3}Fe_{1/3}Mn_{1/3}O_2$ 正极材料中钠离子迁移增强的影响

唐唯佳[1,2,3]，李运姣[1,2,3]，刘彧铭[1,2,3]，雷昌龙[1,2,3]，蒋世杰[1,2,3]，贺振江[1,2,3]

1. 中南大学 冶金与环境学院，长沙 410083；
2. 中南大学 先进电池材料教育部工程研究中心，长沙 410083；
3. 中南大学 低碳有色冶金国家工程研究中心，长沙 410083

摘　要：为了研究 ZrO_2 改性对钠离子电池 $NaNi_{1/3}Fe_{1/3}Mn_{1/3}O_2$(NFM)正极材料电化学性能的影响，通过高温煅烧制备了 ZrO_2 包覆的 NFM (ZrO_2@NFM)。XRD 精修结果表明，ZrO_2 改性增加了 NFM 材料的钠层间距。XPS 结果显示，ZrO_2 改性通过降低 Mn^{3+}含量对 NFM 中 Mn^{3+}/Mn^{4+}的比例进行调整。电化学测试结果表明，与 NFM 相比，ZrO_2@NFM 表现出更优的倍率性能和循环稳定性。同时，ZrO_2@NFM 显著增强了钠离子的扩散系数，降低了界面电荷转移电阻。ZrO_2 涂层增加了钠层间距，减少了电化学极化，抑制了副反应。总之，通过 ZrO_2 涂层的成分调控和表面工程的协同作用，提高了钠离子的扩散动力学，增强了循环稳定性。

关键词：钠离子电池；ZrO_2 涂层；层状氧化物正极材料；扩散系数；电化学性能

(Edited by Wei-ping CHEN)